Check for updates

Mechanistic study of an immobilized molecular electrocatalyst by in situ gap-plasmon-assisted spectro-electrochemistry

Demelza Wright[1,2,6], Qianqi Lin[1,6], Dénes Berta [ID][3,4], Tamás Földes[3,4], Andreas Wagner [ID][2], Jack Griffiths[1], Charlie Readman[1,5], Edina Rosta [ID][3,4 ✉], Erwin Reisner [ID][2 ✉] and Jeremy J. Baumberg [ID][1 ✉]

Immobilized first-row transition metal complexes are potential low-cost electrocatalysts for selective CO_2 conversion in the production of renewable fuels. Mechanistic understanding of their function is vital for the development of next-generation catalysts, although the poor surface sensitivity of many techniques makes this challenging. Here, a nickel bis(terpyridine) complex is introduced as a CO_2 reduction electrocatalyst in a unique electrode geometry, sandwiched by thiol-anchoring moieties between two gold surfaces. Gap-plasmon-assisted surface-enhanced Raman scattering spectroscopy coupled with density functional theory calculations reveals that the nature of the anchoring group plays a pivotal role in the catalytic mechanism. Our in situ spectro-electrochemical measurement enables the detection of as few as eight molecules undergoing redox transformations in individual plasmonic hotspots, together with the calibration of electrical fields via vibrational Stark effects. This advance allows rapid exploration of non-resonant redox reactions at the few-molecule level and provides scope for future mechanistic studies of single molecules.

U nderstanding interface organization and charge transport between materials and molecules is a major issue plaguing the systematic development of photocatalysis, electrochemistry and molecular electronics. An emerging tool for interfacial studies exploits plasmonic gaps constructed from metallic nanostructures[1], which confine optical fields far below the diffraction limit to create a highly localized surface probe with enhanced spectroscopic sensitivity and selectivity. One such plasmonic gap approach is tip-enhanced Raman spectroscopy (TERS), which has been used to observe redox-active molecules responding to electrochemical potential[2,3]. However, the major challenge of reliable fabrication and availability of suitable probes[4], as well as of probe degradation[5], has precluded widespread utilization of TERS. By contrast, although surface-enhanced Raman scattering (SERS)[6–8] at roughened surfaces is easy to implement, it is limited by poor control over surface morphologies that alter electrochemical and spectroscopic behaviours[9]. The high precision of gap-plasmon-assisted SERS (introduced below), which uses metal nanoparticles on an electrode surface[10], is thus becoming a valuable tool in studying real-time in situ redox processes.

While electron transfer at the surface of nanoparticles has been studied electrochemically[11–13], plasmonic nano-gaps enable in situ observation of both oxidized and reduced species through SERS. The high signal-to-noise ratios eliminate the need for electronically resonant enhancement, which is typically susceptible to bleaching over time. These vibrational spectroscopies serve as powerful tools to study catalysis because they provide structural fingerprint information about the catalyst. Of particular interest are immobilized systems[14,15], where molecular catalysts are anchored to surfaces. Understanding these systems is important for designing industrially relevant catalysts, by enhancing performance through improved electron transfer dynamics[16,17], tuning redox mechanisms and improving the long-term stability of catalysts via facile recovery and separation from products[18].

In this work, we perform gap-plasmon-assisted SERS coupled with electrochemistry to study the CO_2 reduction catalyst [Ni(2,2':6',2''-terpyridine-4'-thiol)$_2$](BF$_4$)$_2$ (**Ni(tpyS)$_2$**)[19]. While bis(terpyridine) complexes of cobalt and nickel have previously been used for electrocatalytic CO_2 reduction[19–21], no mechanistic studies have been performed in a sandwich geometry with a highly confined volume. The nickel-centred complex was chosen in this study due to its excellent selectivity for CO_2 reduction towards CO over hydrogen evolution[19–21]. Using in situ SERS between two gold surfaces, we are able to characterize the spectro-electrochemical behaviour, resolving changes in chemical bonding and identifying the catalytic reaction mechanism. Comparison of experimental SERS spectra with density functional theory (DFT) calculations of **Ni(tpyS)$_2$** shows that the first electron transferred during reduction weakens Au–S bonds while the electronic environment of the metal centre changes less, supporting that the nature of the anchoring group plays a pivotal role in the catalytic mechanism. Electrode designs such as confined environments[22] and layered geometries[23,24] advance catalysis by enhancing nanoscale mass transport and electrode dynamics compared to conventional electrodes. We utilize a single-site sandwiched-electrode geometry with a molecular catalyst. Compared to the conventional system with solution-phase nickel catalysts[19,20], this electrode geometry with adsorbed catalyst is likely to change the reaction mechanism as it allows the electron

[1]Nanophotonics Centre, Department of Physics, Cavendish Laboratory, University of Cambridge, Cambridge, UK. [2]Department of Chemistry, University of Cambridge, Cambridge, UK. [3]Department of Chemistry, King's College London, London, UK. [4]Department of Physics and Astronomy, University College London, London, UK. [5]Melville Laboratory for Polymer Synthesis, Department of Chemistry, University of Cambridge, Cambridge, UK. [6]These authors contributed equally: Demelza Wright, Qianqi Lin. ✉e-mail: e.rosta@ucl.ac.uk; reisner@ch.cam.ac.uk; jjb12@cam.ac.uk
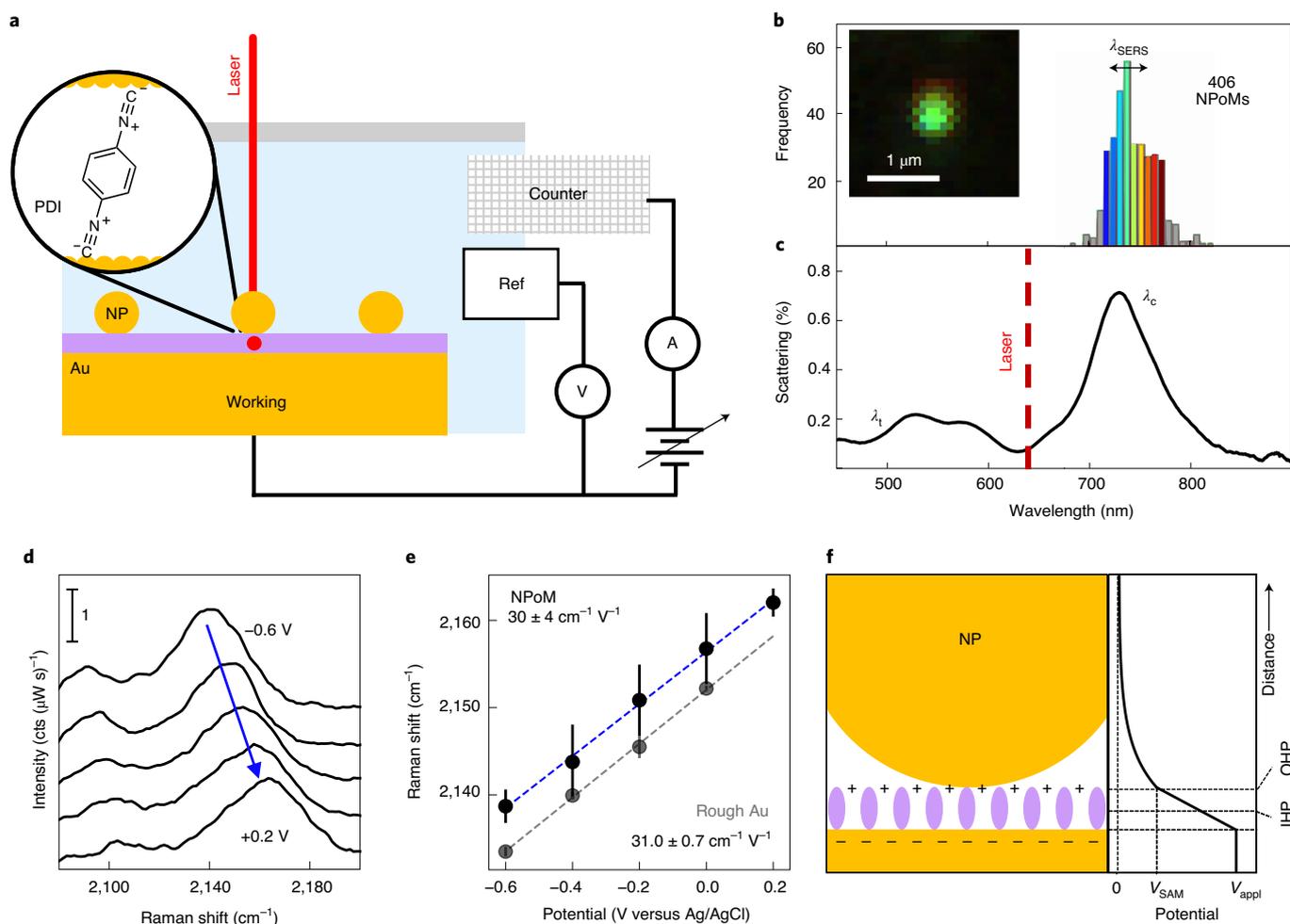
Fig. 1 | Electric field calibration in NPoM. a, NPoM geometry in a spectro-electrochemical cell using three electrodes: gold mirror working electrode (working), platinum counter-electrode (counter) and 3 M KCl Ag/AgCl reference (ref) electrode. Inset: PDI molecule. **b**, Histogram of plasmon-coupled mode positions. The frequency is the number of NPoMs with λ_c occurring in each wavelength bin. Inset: spatial dark-field image of a single 80 nm diameter NPoM. **c**, Dark-field scattering spectrum for PDI monolayer in NPoM. **d**, SERS spectra for PDI in gold nano-gap in aqueous solution with 0.1 M KCl and saturated with N_2, showing $\nu(N\equiv C)$ region at different bias. **e**, Potential-dependent $\nu(N\equiv C)$. Black: NPoMs; grey: roughened gold surface. **d**,**e**, Error bars denote standard deviation; $n=50$ measurements for NPoM, $n=80$ measurements for roughened gold. **f**, Model of electrical double layer in NPoM and potential drop across the gap. NP, nanoparticle; V_{SAM}, the potential at the top of the SAM; V_{appl}, the potential applied by the potentiostat; OHP, outer Helmholtz plane; IHP, inner Helmholtz plane.

gained from reduction to delocalize over the Au–S anchoring unit, inhibits ligand loss and preserves catalyst integrity. This work gives insights into material–molecule hybrid catalysis by going beyond previous work on redox-inactive biphenyl monolayers where changes in molecule polarizability are induced electrochemically[25], or by tracking resonant molecules when they enter and leave electronically active states during redox transitions[26].

Results

Gap-plasmon-assisted spectro-electrochemical assembly. Gap-plasmon cavities have extremely small mode volumes ($<50\,nm^3$) with high optical field enhancements (>500) that strongly amplify the Raman scattering of molecules in the gap by $>10^9$. To construct the nanoparticle-on-mirror (NPoM) plasmonic cavities used here, planar gold substrates are functionalized with a self-assembled monolayer (SAM; Methods). Gold nanoparticles (AuNPs) are then drop-cast on top of the monolayer (Fig. 1a), sandwiching active molecules in the nano-gap. The advantage of this geometry is that the gold mirror conveniently forms one electrode of the cell (Fig. 1a). Dark-field scattering spectra (Fig. 1b,c) on each NPoM

characterize the monolayer quality in the gap. These scattering spectra show transverse (wavelength $\lambda_t \approx 530\,nm$) and coupled (wavelength $\lambda_c \approx 700\,nm$) modes in the NPoM nanocavities. The coupled plasmon at λ_c arises from interaction of the nanoparticle with its image charges in the mirror below, tightly confining the plasmonic hotspot underneath the NPoM[1,27]. The position of λ_c strongly depends on the properties of the gap spacer, including its thickness (d) and effective refractive index (n_g)[28]. Using automated tracking microscopy[29], dark-field scattering spectra are observed for many hundreds of individual NPoMs across the sample surface. Real-time spectro-electrochemical measurements are achieved by incorporating NPoM samples into a three-dimensional (3D)-printed cell. SERS spectra are recorded by illuminating individual NPoMs with a continuous-wave laser at wavelength $\lambda_l = 633\,nm$, with electrochemical potential applied simultaneously to the gold substrate using a three-electrode configuration.

Electric field calibration by vibrational Stark effect. Electrochemical control of the applied potential in the nano-gap was first probed with SERS from a calibration molecule, 1,4-phenylene
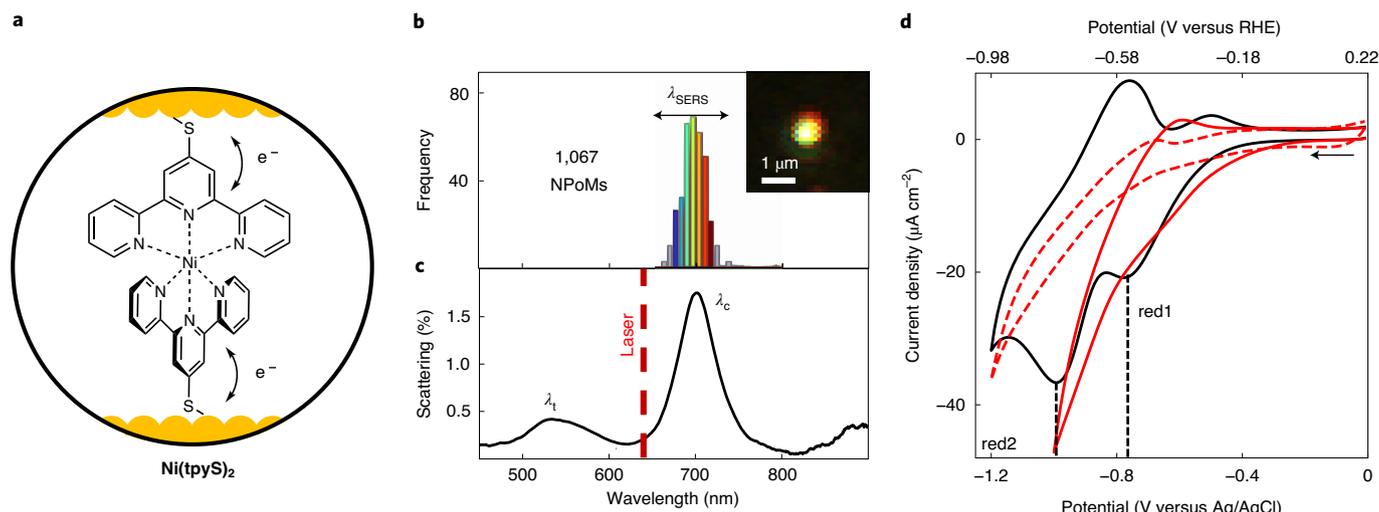
Fig. 2 | Dark-field scattering spectroscopy and electrochemistry for Ni(tpyS)$_2$. a, Ni(tpyS)$_2$ in NPoM geometry. **b**, Histogram of plasmon-coupled mode positions. The frequency is the number of NPoMs with λ_c occurring in each wavelength bin. Inset: spatial image of a single 60 nm diameter NPoM. **c**, Scattering spectra for **Ni(tpyS)$_2$** monolayer in NPoM. **d**, Cyclic voltammograms for NPoMs with (solid lines) or without **Ni(tpyS)$_2$** monolayer (dashed lines) in aqueous solution (pH 3.8) supported with 0.1 M KCl and saturated with N$_2$ (black) or CO$_2$ (red). RHE, reversible hydrogen electrode. Scan rate, 100 mV s^{-1}.

diisocyanide (PDI) (Fig. 1a). Scattering spectra for PDI monolayers are measured from automated tracking of >400 NPoMs (Fig. 1b). These give near-identical coupled modes at $\lambda_c = 739 \pm 22$ nm (Fig. 1c), indicating a highly consistent monolayer over the gold substrate (standard error matches variation in nanoparticle size and shape[30]). Modelling the coupled mode resonance[28] gives $n_{g,PDI} = 1.4$ and $d_{PDI} = 1$ nm, which is consistent with the thickness expected for a monolayer in which the molecules bind to the substrate in a near-vertical rather than flat orientation. SERS spectra for PDI in NPoMs (Fig. 1d) are recorded at potentials ranging from −0.6 to +0.2 V (versus Ag/AgCl) in a N$_2$-saturated aqueous solution with a 0.1 M KCl supporting electrolyte. In this electrochemically inert range for PDI (Supplementary Fig. 1), the SERS band near 2,130 cm^{-1} shows a large blue shift as positive potential is applied, shifting linearly at 30 ± 4 cm^{-1} V^{-1} (Fig. 1e, black). This is consistent with the stretching mode (ν) for isocyanide (N≡C) bound to the gold surface[31]. For comparison, SERS spectra for PDI at electrochemically roughened gold surfaces are recorded and analysed (Fig. 1e, grey) under the same conditions, where ν(N≡C) shifts by 31 ± 1 cm^{-1} V^{-1}.

These SERS shifts arise from the vibrational Stark effect (VSE)[31–33], where the vibrational energies of chemical bonds are perturbed by an electric field. The frequency (Stark) shift versus potential, known as the Stark tuning rate, enables direct measurement of the potential gradient at the electrode. Our measurements provide direct evidence that the electrochemical potential gradient (that is, electric field) at the NPoM surface of a SAM is identical to that found at a roughened electrode surface of a SAM. While electron tunnelling has been reported across NPoM plasmonic gaps, the electron transfer process at the interface between the SAM and this sandwiched electrode geometry remains unclear[12,13]. To address this question, a model of the electrical double layer[31,34] for the NPoM junction (Fig. 1f) is developed here. Because the SAM is adsorbed on the gold substrate, the electrical centre of the monolayer is the inner Helmholtz plane (IHP). Solvated ions from the supporting electrolyte approach the SAM by diffusion, and the position of these nearest ions is the outer Helmholtz plane (OHP), roughly corresponding to the length of molecules ($d \approx 1$ nm). Following double-layer capacitive (non-Faradaic) charging, the potential drops rapidly within

the OHP. Faradaic electron transfer takes place readily between the gold substrate and the monolayer (as observed below). This electron transfer process is similar to the case when no nanoparticle is on top of the SAM, implying that electron tunnelling is not the only path across the gaps, otherwise the VSE should not be observed. In fact, electron tunnelling is less efficient due to the 1-nm barrier width[35] and hence an electron transfer process through the SAM dominates (Supplementary Fig. 2).

Spectro-electrochemical studies of immobilized Ni(tpyS)$_2$. Using **Ni(tpyS)$_2$** in the nano-gap (Fig. 2a) allows tracking of redox and catalytic reactions. Scattering spectra for the **Ni(tpyS)$_2$** monolayer measured from >1,000 NPoMs (Fig. 2b,c) shows the coupled mode at $\lambda_c = 696 \pm 15$ nm, confirming that the monolayer is uniform with $n_{g,\mathbf{Ni(tpyS)}_2} = 1.4$ and $d_{\mathbf{Ni(tpyS)}_2} = 1.5$ nm. A dark-field image (Supplementary Fig. 3) demonstrates the spatially well-separated nanoparticle distribution. Cyclic voltammetry (CV) for **Ni(tpyS)$_2$** NPoMs is first recorded in a N$_2$-saturated aqueous solution (pH 3.8) supported with 0.1 M KCl, from 0 to −1.2 V (versus Ag/AgCl) and back to 0 V (Fig. 2d, black). Two reductive waves are observed: red1 at $E_p = -0.76$ V and red2 at $E_p = -0.99$ V, corresponding to the first and second reductions, respectively, of **Ni(tpyS)$_2$** (refs. [19,20]). These electrochemical responses are markedly different from the voltammogram produced when no nanoparticle is on top of the Au-**Ni(tpyS)$_2$** monolayer (Supplementary Fig. 4, blue). In the absence of AuNPs, the absence of oxidative waves indicates that the redox process is chemically irreversible. This may in part be due to the loss of one tpyS ligand. By contrast in the NPoM construct, the presence of two oxidative waves supports a chemically reversible process, confirming preservation of the two tpyS ligands coordinated to the nickel centre. The voltammetric features of **Ni(tpyS)$_2$** are considerably clearer, indicating that the voltammogram is dominated by the molecules underneath the nanoparticles rather than the exposed monolayer. As a result, the CV directly measures conditions in the gap. More importantly, while a broad wave at −0.86 V is observed in the absence of the nanoparticle on top (Supplementary Fig. 4, blue), the presence of nanoparticles shows a well-defined reductive wave shifting by +0.1 V (Supplementary Fig. 4, black). This can be explained by reduction of the monolayer becoming
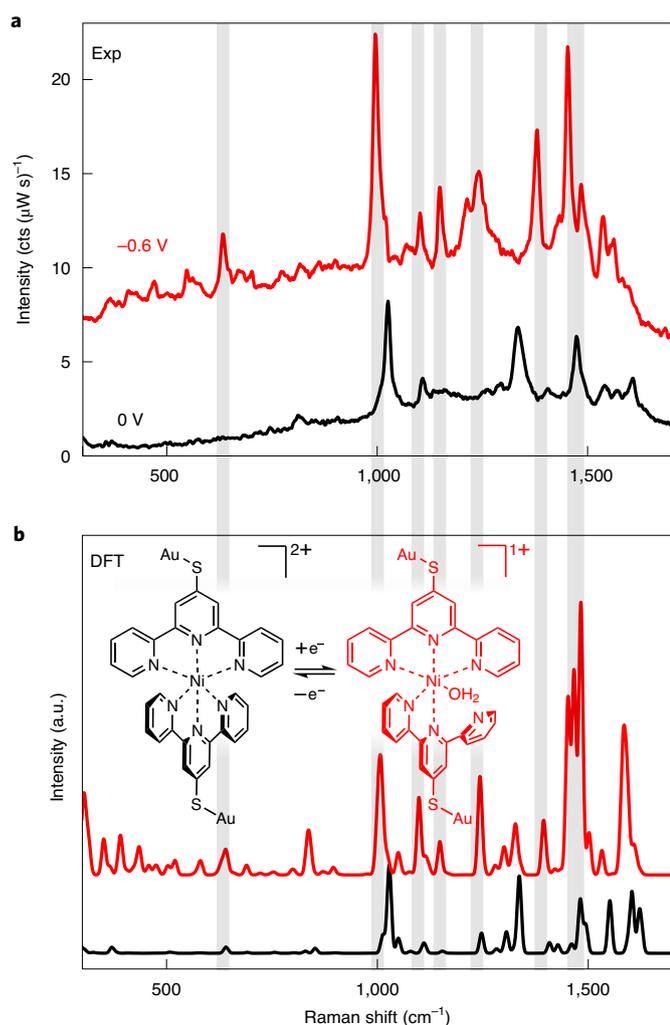
Fig. 3 | SERS and DFT calculations for Ni(tpyS)₂. a, Experimental (exp) SERS spectra of **Ni(tpyS)₂** in NPoM at 0 V (black) and −0.6 V (red, difference spectrum) versus Ag/AgCl in aqueous solution (pH 3.8) supported with 0.1 M KCl and saturated with N₂. Additional bands appearing at −0.6 V are highlighted in grey. **b**, DFT-calculated Raman spectra for **[Ni(tpyS)₂]²⁺** (black) and **[Ni(tpyS)₂–H₂O]¹⁺** (red). a.u., arbitrary units.

To avoid proton reduction[25], which forms bubbles that disrupt optical measurements, potentials are kept at −0.6 V to observe **Ni(tpyS)₂** in the first reduced state only. Comparison of these spectra shows that during reduction, the SERS background increases and several spectral bands emerge (highlighted in grey in Fig. 2d). Despite attenuation and scattering from the spectro-electrochemical cell, SERS signals exceed 10 cts (µW s)⁻¹ (cts, counts) with a high signal-to-noise ratio. While **Ni(tpyS)₂** is electronically non-resonant at $\lambda_1 = 633$ nm (Supplementary Fig. 5 shows no absorption/emission at λ_1, which is essential for correct measurement of electrochemical performance), the near-resonant plasmonic mode at 696 nm strongly enhances the SERS (Fig. 2c). Similar measurements for **Ni(tpyS)₂** on an electrochemically roughened gold substrate (Supplementary Fig. 6) show spectral changes in the reduced $[Ni(tpyS)_2]^{1+}$ state, though with broader, less-defined SERS bands with an order of magnitude lower intensity.

DFT Raman calculations are performed to simulate the SERS responses for **Ni(tpyS)₂** in different redox states. Comparison of computational spectra with experimental SERS for $[Ni(tpyS)_2]^{2+}$ (black lines Fig. 3a,b) shows excellent agreement. We consider several possible reduction products for bis(terpyridine) complexes involving different mechanisms, including those in refs. [19,21]. The calculated Raman spectra (Supplementary Fig. 7) show that $[Ni(tpyS)_2–H_2O]^{1+}$ involving a one-electron reduction of the ligand, and the addition of a water molecule to the nickel coordination, gives the best agreement with experiments (red lines in Fig. 3). The spectral bands are labelled with relevant vibrational modes and are discussed in Supplementary Fig. 8 and Supplementary Note 1. Further DFT calculations considering the effects of the electrical double layer on the polarization of dipoles (Supplementary Fig. 9) show the same spectral matching results as calculations from isotropic and unpolarized environments. The first reduction process red1 (Fig. 2d) is thus identified as the electron transfer step, where 'ads' and 'aq' refer to the adsorbed and aqueous phases, respectively:

$$[Ni(tpyS)_2]^{2+}(ads) + e^- + H_2O(aq) \rightleftharpoons [Ni(tpyS)_2–H_2O]^{1+}(ads)$$
(1)
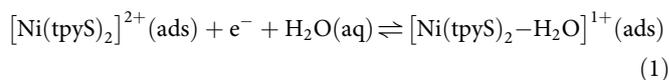
The reduction process for the dissolved non-thiolated catalyst, $[Ni(2,2':6',2''-terpyridine)_2](BF_4)_2$ (**Ni(tpy)₂**), has been suggested to accompany the loss of one terpyridine ligand to form an active mono(terpyridine) complex[19,20]. With the unique sandwiched electrode geometry and thiolated catalyst here, the mono(terpyridine)–nickel complex was not observed in our spectra (Supplementary Fig. 7). Rather, the calculated charge distribution shows that the single electron gained from reduction is not localized at the metal centre and instead perturbs the Au–S bond (Supplementary Fig. 10). This is consistent with the reported electrochemistry for nickel-centred bis(terpyridine) complexes, where ligand-based redox dominates[20] due to the relative stability of the Ni²⁺ d⁸ outer shell electron configuration.

In addition to weakening the Au–S bond, DFT calculations also show that bond orders for the coordination bonds are affected (Supplementary Table 1). The axial Ni–N bonds on both tpyS ligands are strengthened, but the equatorial Ni–N bonds are weakened, during reduction. Since partial ligand exchange is thermodynamically favourable when the complex is reduced, solvent access to the nickel centre for coordination is proposed. This is confirmed by comparison of calculated and experimental spectra of the reduced state by a discrete implementation of earth mover's algorithm (Supplementary Note 2), whereby we find a substantial improvement in spectral agreement when including a coordinated water molecule (Supplementary Fig. 7). Since the complexes are octahedral, at least one of the existing coordination bonds must be broken to allow CO₂ binding to the metal centre for subsequent catalytic
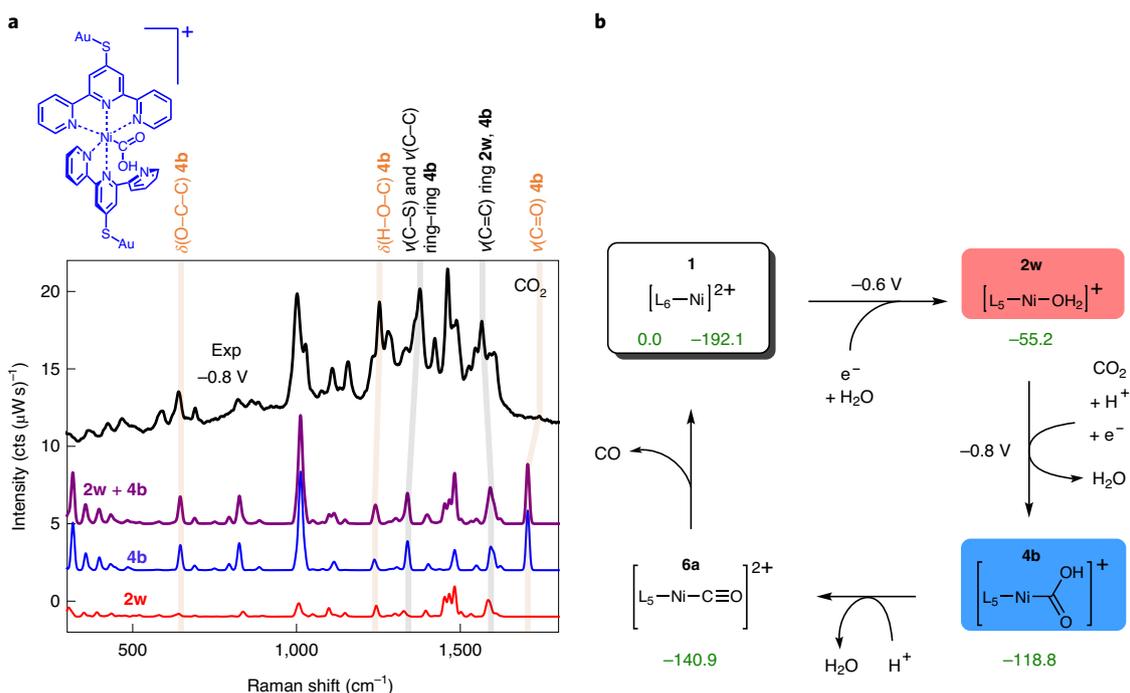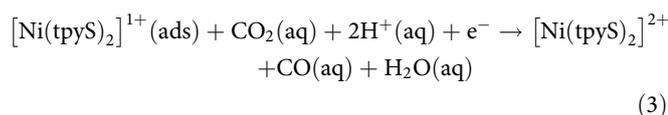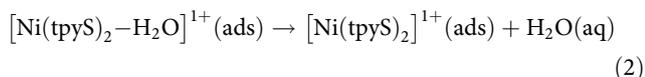
thermodynamically more favourable, due to stabilization of the reduced radical species via adsorption by the nanoparticle on top (Supplementary Fig. 4d)[36]. The nanoparticle further stabilizes the adsorbed system by withdrawing electron density from the monolayer, making reduction easier. This stabilization is not molecule specific, because for PDI the $\nu(N\equiv C)$ shifts by −5 cm⁻¹ in NPoMs versus a rough gold electrode (Fig. 1e). NPoM plasmonic cavities thus considerably enhance interfacial electron transfer.

The CV for CO₂ catalytic reduction is recorded in a CO₂-saturated solution with **Ni(tpyS)₂** NPoMs (Fig. 2d, red solid lines), and compared with CO₂ reduction on the gold substrate without the **Ni(tpyS)₂** monolayer in the same solution (Fig. 2d, red dashed lines). Comparison of these shows over twofold increased current density with the onset potential shifting to −0.52 V, illustrating that the electrocatalytic CO₂ reduction is mediated by **Ni(tpyS)₂** NPoMs before proton reduction on gold[25].

Surface-enhanced Raman scattering is now used to explore chemical bonding changes. SERS spectra (Fig. 3a) are recorded for both the reduced state ($[Ni(tpyS)_2]^{1+}$, −0.6 V) and oxidized state ($[Ni(tpyS)_2]^{2+}$, 0 V versus Ag/AgCl, according to the CV in Fig. 2d).

Fig. 4 | Ni(tpyS)₂-catalysed CO₂ reduction. a, Experimental (exp) SERS of **Ni(tpyS)₂** averaged from different NPoMs in CO₂-saturated aqueous solution (pH 3.8) at −0.8 V, and DFT-calculated, best-matched purple spectrum. The latter is derived from linear combination of the red and blue spectra, corresponding to their colour-shaded intermediates, respectively, in **b**. Grey bars highlight matching spectral bands between experiments and calculations. Vibrational modes relevant to CO₂ reduction are highlighted in orange; more vibrational modes are shown in Supplementary Figs. 8 and 15. **b**, Proposed catalytic cycle of **Ni(tpyS)₂**-mediated CO₂ reduction. Relative Gibbs free energies (kcal mol⁻¹) are displayed in green. Shaded intermediates are spectroscopically verified. L_n represents tpyS ligands forming n Ni–N bonds. $[L_6–Ni]^{2+} = [Ni(tpyS)_2]^{2+}$, $[L_5–Ni-H_2O]^{1+} = [Ni(tpyS)_2–H_2O]^{1+}$.

reduction. Our experiments and computations strongly support that this reaction is realized through the breaking of a single Ni–N bond followed by rotation of a pyridine unit from one tpyS ligand. (Supplementary Fig. 7).

Mechanistic studies of Ni(tpyS)₂-mediated CO₂ reduction. Performing SERS in the presence of CO₂, several new spectral modes emerge (Fig. 4a, black). Gibbs energies (Supplementary Table 3 and Supplementary Fig. 11) and Raman spectra (Supplementary Fig. 12) were calculated for 22 different reaction intermediates (Supplementary Note 3 and Supplementary Table 2). Experimental SERS measurements were compared with DFT-calculated single and combined Raman spectra obtained as a mixture of two or three intermediates (Supplementary Fig. 13 and Supplementary Table 4). In calculations, the effect of electron transfer was estimated based on the measured half-cell potentials. The proposed catalytic 2H⁺/2e⁻ reduction of CO₂ overall is:

$$\left[Ni(tpyS)_2 - H_2O\right]^{1+}(ads) \rightarrow \left[Ni(tpyS)_2\right]^{1+}(ads) + H_2O(aq) \quad (2)$$

$$\left[Ni(tpyS)_2\right]^{1+}(ads) + CO_2(aq) + 2H^+(aq) + e^- \rightarrow \left[Ni(tpyS)_2\right]^{2+} + CO(aq) + H_2O(aq) \quad (3)$$

where equation (2) illustrates the creation of a vacant site on $[Ni(tpyS)_2]^{1+}$ as H₂O dissociates. We have explored the possible intermediates for all possible orders of electron and proton transfer steps (Supplementary Table 2). Spectra from only the most

feasible structures, according to calculated Gibbs and electronic energies, were used for spectral matches (Supplementary Fig. 12). Deprotonated carboxyl groups bound to the nickel centre have been reported as intermediates in bis(terpyridine) complexes catalysing CO₂ reduction[19,37]. We performed geometry optimizations for structures where we removed the proton covalently bonded to CO₂ (Supplementary Fig. 14). Most of these calculations show CO₂ detachment from the complex. For the only successfully converged structure, the reaction relative free energy for deprotonation was calculated as +10 kcal mol⁻¹, and thus the intermediate is less stable when deprotonated. This free energy can be interpreted as a pK_a of 7.3, while the experiments were performed at pH 3.8, confirming that the carboxyl group is protonated. Further calculations find pK_a of the pendant pyridyl group as −9.3 for **[Ni(tpyS)₂-H₂O]¹⁺**, which is not equivalent to the free unsubstituted ligand in solution[38] (see Supplementary Table 5 and Supplementary Note 4). Despite the similarity of the molecules to those recorded in the literature, bis(terpyridine) ligands have been used as homogeneous systems where a terpyridine has been proposed to dissociate after its first reduction. We note a mechanism without ligand displacement has previously only been proposed for a phosphonated Co (bis)terpyridine catalyst on a metal oxide electrode[21]. Our work is performed in a confined environment, with two Au–S anchoring points imposing electronic and steric constraints on the system giving distinctive pK_a and intermediates.

The best spectral match under CO₂ conditions (Fig. 4a, purple) is a linear combination of two different species (Fig. 4a, red and blue) that correspond to the shaded intermediates in Fig. 4b. Vibrational modes of these intermediates are assigned and discussed in Supplementary Note 5 and Supplementary Figs. 8 and 15. ν(C=O) is low intensity and absent from some NPoMs, due to weak enhancement when C=O is near perpendicular to the gap

optical field (in the DFT, unpolarized excitations are used). We find (Supplementary Table 4) that 75% of the spectral contribution is derived from **2w** ($[L_5\text{-Ni-OH}_2]^{1+}$; see full structure in Fig. 3b, red) and 25% is from **4b** ($[L_5\text{-Ni-COOH}]^{1+}$); see full structure in Fig. 4a, blue). Using the size of individual nanostructures and single molecules, the number of molecules in the plasmonic hotspot can be estimated geometrically as 32 (Supplementary Note 6). Combining these numbers, we are able optically to detect and identify approximately eight molecules undergoing catalytic turnover. Consecutive SERS spectra with real-time chronoamperometry (Supplementary Fig. 6) show more stochastic behaviour of reduction onset for NPoM samples compared with electrochemically roughened gold, as expected for the few-molecule regime.

A catalytic cycle is proposed (Fig. 4b) based on combined spectroscopic and computational results. Following the initial reduction and Ni–N bond breaking, the water-coordinated species $[L_5\text{-Ni-OH}_2]^{1+}$ is formed. The water molecule is highly labile and creates a vacant site on the nickel centre as it dissociates. After the second reduction step, the nickel centre is sufficiently nucleophilic to attack the CO_2 carbon atom, forming CO as the catalytic product. Supplementary Fig. 16 and Supplementary Note 7 contain further discussion.

Conclusions

We have introduced an electrode geometry for in situ spectroelectrochemical SERS measurement with excellent signal-to-noise ratios owing to gap-plasmon enhancements. We spectroscopically track the redox transitions of as few as eight molecules, showing that single-molecular catalyst spectroscopy is within reach. The electrochemical properties of the NPoM electrode are compared with the standard roughened gold electrode via the vibrational Stark effect, finding that NPoM is a promising electrode geometry for surface-bound species. Utilizing this electrode, we probe the electrocatalytic mechanism of CO_2 reduction by the molecular catalyst **Ni(tpyS)₂**. Through virtual screening of intermediates in combination with SERS, we identify a reaction pathway that involves an anchoring group-based intermediate species, emphasizing that the nature of the anchoring group can play a pivotal role in surface-bound catalysis. This electrode geometry successfully tunes the catalytic reaction mechanism by preventing ligand loss and hence facilitates facile recovery of the catalyst.

Methods

Assembly of Ni(tpyS)₂. All chemicals were purchased from Sigma-Aldrich, unless stated otherwise, at the highest purity available and used as received. **Ni(tpyS)₂** is the abbreviation for [Ni(2,2':6',2"-terpyridine-4'-thiol)₂](BF₄)₂. It was assembled by a previously reported procedure[19]. 2,2':6',2"-terpyridine-4'-thiol (tpyS) was purchased from HetCat (Switzerland) and Ni(BF₄)₂.6H₂O was purchased from Acros Organics.

Electrode preparation. Gold electrodes were fabricated by the template-stripping method as reported elsewhere[39]. **Ni(tpyS)₂** SAMs were formed by immersing gold electrodes in a 1 mM **Ni(tpyS)₂** acetonitrile solution for 22 h, rinsing with acetonitrile and drying with compressed N₂. Standard AuNPs in a citrate buffer were purchased from BBI Solutions[36] (60 and 80 nm) with reported morphology[10]. AuNPs were deposited by drop-casting AuNP solution onto the sample for 20 s, rinsing with distilled water and drying with compressed N₂. Electrochemically roughened gold electrodes were made using an established oxidation and reduction cycling method[40]. Gold films were immersed in 0.1 M KCl and potentiostatted at −0.6 V versus Ag/AgCl for 10 s, then swept to 1.1 V and held at this potential for 2 s. The samples were swept back to −0.6 V and these steps were repeated 25 times. A **Ni(tpyS)₂** monolayer was formed as above.

Spectro-electrochemical cell. A specially designed three-electrode 3D-printed cell is used for all spectro-electrochemical measurements. NPoM samples are used as the working electrode, a platinum mesh (Alfa Aesar) as counter-electrode and Ag/AgCl (3 M KCl, eDAQ ET072, Green Leaf Scientific) as reference electrode. The cell is closed by a 25 × 25 × 0.2 mm³ glass coverslip. Sample to coverslip distance is approximately 0.3 mm, to allow high-numerical-aperture (NA) collection of SERS scattering. Electrochemical measurements were recorded on either a CompactStat (Ivium Technologies) or an Autolab PGSTAT204 (Metrohm).

SERS collection. SERS measurements were recorded on a modified Olympus BX51 coupled to a 633-nm laser set at powers <100 μW. Excitation and collection were performed through an Olympus MPLFLN100xBD 0.9-NA objective. Spectra were recorded by an Andor camera coupled to a Triax 320 spectrometer.

Dark-field scattering spectroscopy. Dark-field spectroscopy was performed on a modified Olympus BX51 coupled to an incoherent white light source. Excitation and collection were through a 0.8-NA Olympus LWD BF/DF objective. Spectra were recorded on a fibre-coupled OceanOptics QE65000. Automated scans were performed using a Python particle-tracking code[29]. A standard diffuser was used as a reference to normalize white light scattering.

Ultraviolet–visible collection. Ultraviolet–visible (UV–vis) spectra were recorded on a Cary 50 (Varian) with a quartz UV–vis cuvette (Fisher).

DFT calculations. Absorbed **Ni(tpyS)₂** molecules were modelled as thiol groups anchored to single gold atoms on both ends. DFT from a single Au atom shows an excellent match with the experimental SERS[41] at a much lower computational cost compared to DFT from large Au clusters[17,31], and is sufficient to describe any charge transfer to the molecules. Although Ni(II) can form square planar and tetrahedral complexes, bis(terpyridine) ligands form strong octahedral coordination due to steric considerations[42]. DFT optimization performed for $[\text{Ni(tpyS)}_2]^{2+}$ gives a clear preference for the tetrahedral rather than the square planar, by a relative free energy of −24.4 kcal mol⁻¹. Both the literature and DFT optimization confirm this geometry. Geometric optimizations and frequency calculations were performed with the B3LYP[43] hybrid functional and def2SVP basis sets, including core potentials as implemented in Gaussian09 Revision E[44]. Non-covalent interactions were corrected using Grimme's dispersion correction v.3 with Becke–Johnson damping[45]. Charge distribution and bond indices were calculated using the natural bond analysis package[46,47]. Free energies were estimated based on single-point electronic energies calculated with the def2TZVPP[48] basis set, thermal corrections were obtained using RRHO approximation and solvent correction was incorporated with polarizable continuum model solvation using the solvation model based on density (SMD) parametrization[49]. Stability of wave functions was ensured in all cases. Free energy corrections were introduced for both reduction steps as $\Delta G = eV$ (ΔG, Gibbs free energy; e, elemental charge; V, potential), and the cost of protonation was calculated for pH 3.8 based on the experimental free energy of a solvated proton[50]. Computational spectra were scaled by a factor of 0.978 to match with the experiment. Further details on matching are available in Supplementary Note 2.

Data availability
The data that support the findings of this study are available from the University of Cambridge data repository at https://doi.org/10.17863/CAM.60379.

Code availability
The code for spectral matching using the earth mover algorithm is available from the University of Cambridge data repository at https://doi.org/10.17863/CAM.60379.

References

1. Baumberg, J. J., Aizpurua, J., Mikkelsen, M. H. & Smith, D. R. Extreme nanophotonics from ultrathin metallic gaps. *Nat. Mater.* **18**, 668–678 (2019).
2. Pfisterer, J. H. K. & Domke, K. F. Unfolding the versatile potential of EC-TERS for electrocatalysis. *Curr. Opin. Electrochem.* **8**, 96–102 (2018).
3. Kang, G., Yang, M., Mattei, M. S., Schatz, G. C. & Van Duyne, R. P. *In situ* nanoscale redox mapping using tip-enhanced Raman spectroscopy. *Nano Lett.* **19**, 2106–2113 (2019).
4. Schmid, T., Opilik, L., Blum, C. & Zenobi, R. Nanoscale chemical imaging using tip-enhanced Raman spectroscopy: a critical review. *Angew. Chem. Int. Ed.* **52**, 5940–5954 (2013).
5. Kumar, N. et al. Extending the plasmonic lifetime of tip-enhanced Raman spectroscopy probes. *Phys. Chem. Chem. Phys.* **18**, 13710–13716 (2016).
6. Wu, D.-Y., Li, J.-F., Ren, B. & Tian, Z.-Q. Electrochemical surface-enhanced Raman spectroscopy of nanostructures. *Chem. Soc. Rev.* **37**, 1025–1041 (2008).
7. Zong, C., Chen, C. J., Zhang, M., Wu, D. Y. & Ren, B. Transient electrochemical surface-enhanced Raman spectroscopy: a millisecond time-resolved study of an electrochemical redox process. *J. Am. Chem. Soc.* **137**, 11768–11774 (2015).
8. Wain, A. J. & O'Connell, M. A. Advances in surface-enhanced vibrational spectroscopy at electrochemical interfaces. *Adv. Phys. X* **2**, 188–209 (2017).
9. Willets, K. A. & Van Duyne, R. P. Localized surface plasmon resonance spectroscopy and sensing. *Annu. Rev. Phys. Chem.* **58**, 267–297 (2007).

10. Benz, F. et al. SERS of individual nanoparticles on a mirror: size does matter, but so does shape. *J. Phys. Chem. Lett.* **7**, 2264–2269 (2016).

11. Chazalviel, J.-N. & Allongue, P. On the origin of the efficient nanoparticle mediated electron transfer across a self-assembled monolayer. *J. Am. Chem. Soc.* **133**, 762–764 (2011).

12. Zhao, J., Bradbury, C. R. & Fermín, D. J. Long-range electronic communication between metal nanoparticles and electrode surfaces separated by polyelectrolyte multilayer films. *J. Phys. Chem. C* **112**, 6832–6841 (2008).

13. Shein, J. B., Lai, L. M. H., Eggers, P. K., Paddon-Row, M. N. & Gooding, J. J. Formation of efficient electron transfer pathways by adsorbing gold nanoparticles to self-assembled monolayer modified electrodes. *Langmuir* **25**, 11121–11128 (2009).

14. Wang, L., Polyansky, D. E. & Concepcion, J. J. Self-assembled bilayers as an anchoring strategy: catalysts, chromophores, and chromophore-catalyst assemblies. *J. Am. Chem. Soc.* **141**, 8020–8024 (2019).

15. Dalle, K. E. et al. Electro- and solar-driven fuel synthesis with first row transition metal complexes. *Chem. Rev.* **119**, 2752–2875 (2019).

16. Materna, K. L., Crabtree, R. H. & Brudvig, G. W. Anchoring groups for photocatalytic water oxidation on metal oxide surfaces. *Chem. Soc. Rev.* **46**, 6099–6110 (2017).

17. Clark, M. L. et al. CO_2 reduction catalysts on gold electrode surfaces influenced by large electric fields. *J. Am. Chem. Soc.* **140**, 17643–17655 (2018).

18. Cunillera, A. et al. Highly efficient Rh-catalysts immobilised by π-π stacking for the asymmetric hydroformylation of norbornene under continuous flow conditions. *ChemCatChem* **11**, 2195–2205 (2019).

19. Kuehnel, M. F., Orchard, K. L., Dalle, K. E. & Reisner, E. Selective photocatalytic CO_2 reduction in water through anchoring of a molecular Ni catalyst on CdS nanocrystals. *J. Am. Chem. Soc.* **139**, 7217–7223 (2017).

20. Elgrishi, N., Chambers, M. B., Artero, V. & Fontecave, M. Terpyridine complexes of first row transition metals and electrochemical reduction of CO_2 to CO. *Phys. Chem. Chem. Phys.* **16**, 13635–13644 (2014).

21. Leung, J. J. et al. Solar-driven reduction of aqueous CO_2 with a cobalt bis(terpyridine)-based photocathode. *Nat. Catal.* **2**, 354–365 (2019).

22. Bae, J. H., Han, J.-H. & Chung, T. D. Electrochemistry at nanoporous interfaces: new opportunity for electrocatalysis. *Phys. Chem. Chem. Phys.* **14**, 448–463 (2012).

23. Ai, L., Tian, T. & Jiang, J. Ultrathin graphene layers encapsulating nickel nanoparticles derived metal–organic frameworks for highly efficient electrocatalytic hydrogen and oxygen evolution reactions. *ACS Sustain. Chem. Eng.* **5**, 4771–4777 (2017).

24. Yang, Y., Liu, Z. & Lian, T. Bulk transport and interfacial transfer dynamics of photogenerated carriers in CdSe quantum dot solid electrodes. *Nano Lett.* **13**, 3678–3683 (2013).

25. Di Martino, G. et al. Tracking nanoelectrochemistry using individual plasmonic nanocavities. *Nano Lett.* **17**, 4840–4845 (2017).

26. Jiang, S. et al. Investigation of cobalt phthalocyanine at the solid/liquid interface by electrochemical tip-enhanced Raman spectroscopy. *J. Phys. Chem. C* **123**, 9852–9859 (2019).

27. Olalla, P. Optical transport and sensing in plexcitonic nanocavities. *Opt. Express* **21**, 2649–2654 (2013).

28. Benz, F. et al. Generalized circuit model for coupled plasmonic systems. *Opt. Express* **23**, 33255–33269 (2015).

29. De Nijs, B. et al. Unfolding the contents of sub-nm plasmonic gaps using normalising plasmon resonance spectroscopy. *Faraday Discuss.* **178**, 185–193 (2015).

30. Gold nanoparticles. *BBI Solutions* https://bbisolutions.com/en/products/gold-reagents/gold-nanoparticles.html (2020).

31. Ge, A. et al. Interfacial structure and electric field probed by *in situ* electrochemical vibrational Stark effect spectroscopy and computational modeling. *J. Phys. Chem. C* **121**, 18674–18682 (2017).

32. Boxer, S. G. Stark realities. *J. Phys. Chem. B* **113**, 2972–2983 (2009).

33. Nelson, D. A. & Schultz, Z. D. Influence of optically rectified electric fields on the plasmonic photocatalysis of 4-nitrothiophenol and 4-aminothiophenol to 4,4-dimercaptoazobenzene. *J. Phys. Chem. C* **122**, 8581–8588 (2018).

34. Compton, R. G. & Banks, C. E. *Understanding Voltammetry* (Imperial College Press, 2010).

35. Akkerman, H. B. et al. Electron tunneling through alkanedithiol self-assembled monolayers in large-area molecular junctions. *Proc. Natl Acad. Sci. USA* **104**, 11161–11166 (2007).

36. Poon, J. et al. Altered electrochemistry at graphene- or alumina-modified electrodes: catalysis vs electrocatalysis in multistep electrode processes. *J. Phys. Chem. C* **119**, 13777–13784 (2015).

37. Hu, Y. et al. Tracking mechanistic pathway of photocatalytic CO_2 reaction at Ni sites using operando time-resolved spectroscopy. *J. Am. Chem. Soc.* **142**, 5618–5626 (2020).

38. Farkas, E., Enyedy, É. A., Micera, G. & Garribba, E. Coordination modes of hydroxamic acids in copper(II), nickel(II) and zinc(II) mixed-ligand complexes in aqueous solution. *Polyhedron* **19**, 1727–1736 (2000).

39. Readman, C. et al. Anomalously large spectral shifts near the quantum tunnelling limit in plasmonic rulers with subatomic resolution. *Nano Lett.* **19**, 2051–2058 (2019).

40. Liu, Y. C., Hwang, B. J. & Jian, W. J. Effect of preparation conditions for roughening gold substrate by oxidation-reduction cycle on the surface-enhanced Raman spectroscopy of polypyrrole. *Mater. Chem. Phys.* **73**, 129–134 (2002).

41. Carnegie, C. et al. Room-temperature optical picocavities below 1 nm³ accessing single-atom geometries. *J. Phys. Chem. Lett.* **9**, 7146–7151 (2018).

42. Anderer, C., Näther, C. & Bensch, W. Bis(2,2':6',2"-terpyridine-K³ N,N',N") nickel(II) bis(perchlorate) hemihydrate. *IUCrData* **1**, x161009 (2016); https://iucrdata.iucr.org/x/issues/2016/07/00/su4053/su4053.pdf

43. Becke, A. D. Density−functional thermochemistry. III. The role of exact exchange. *J. Chem. Phys.* **98**, 5648–5652 (1993).

44. Frisch, M. J. et al. Gaussian 09, Revision E (Gaussian, 2009).

45. Grimme, S., Ehrlich, S. & Goerigk, L. Effect of the damping function in dispersion corrected density functional theory. *J. Comput. Chem.* **32**, 1456–1465 (2011).

46. Foster, J. P. & Weinhold, F. Natural hybrid orbitals. *J. Am. Chem. Soc.* **102**, 7211–7218 (1980).

47. Reed, A. E., Curtiss, L. A. & Weinhold, F. Intermolecular interactions from a natural bond orbital, donor-acceptor viewpoint. *Chem. Rev.* **88**, 899–926 (1988).

48. Weigend, F. & Ahlrichs, R. Balanced basis sets of split valence, triple zeta valence and quadruple zeta valence quality for H to Rn: design and assessment of accuracy. *Phys. Chem. Chem. Phys.* **7**, 3297–3305 (2005).

49. Marenich, A. V., Cramer, C. J. & Truhlar, D. G. Universal solvation model based on solute electron density and on a continuum model of the solvent defined by the bulk dielectric constant and atomic surface tensions. *J. Phys. Chem. B* **113**, 6378–6396 (2009).

50. Tissandier, M. D. et al. The proton's absolute aqueous enthalpy and Gibbs free energy of solvation from cluster-ion solvation data. *J. Phys. Chem. A* **102**, 7787–7794 (1998).

Acknowledgements

Author contributions

D.W., Q.L., E. Reisner and J.J.B. conceived the research and developed the experiments. D.B., T.F. and E. Rosta carried out DFT calculations and provided input on catalytic interpretation. A.W. and E. Reisner provided input on interpretation of electrochemical and catalytic results. J.G. helped with spectral analysis. C.R. helped with synthesis of **Ni(tpyS)**$_2$. D.W., Q.L., D.B., T.F. and J.J.B. analysed the data and wrote the manuscript with input from all authors.

Competing interests

The authors declare no competing interests.

Additional information